Journal of Magnetic Resonance 312 (2020) 106686

Contents lists available at ScienceDirect

Journal of Magnetic Resonance

journal homepage: www.elsevier.com/locate/jmr

High Xe density, high photon flux, stopped-flow spin-exchange optical pumping: Simulations versus experiments

Jason G. Skinner [a,1], Kaili Ranta [b,2], Nicholas Whiting [c], Aaron M. Coffey [d], Panayiotis Nikolaou [e], Matthew S. Rosen [f,g,h], Eduard Y. Chekmenev [i,j], Peter G. Morris [k], Michael J. Barlow [a], Boyd M. Goodson [b,*]

[a] Division of Respiratory Medicine, School of Medicine, Queen's Medical Centre, University of Nottingham, Nottingham, NG7 2UH, UK
[b] Department of Chemistry and Biochemistry, Southern Illinois University Carbondale, Carbondale, IL, 62901, USA
[c] Department of Physics & Astronomy and Department of Molecular & Cellular Biosciences, Rowan University, Glassboro, NJ 08028, USA
[d] Vanderbilt University Institute of Imaging Science (VUIIS), Department of Radiology and Radiological Sciences, Vanderbilt-Ingram Cancer Center (VICC), Department of Biomedical Engineering, Department of Physics and Astronomy, Vanderbilt University Medical Center, Nashville, TN, 37232, USA
[e] XeUS Technologies LTD, Pano Lakatamia, Nicosia 2312, Cyprus
[f] Athinoula A. Martinos Center for Biomedical Imaging, Department of Radiology, Massachusetts General Hospital, 149 13th Street, Charlestown, MA 02129, USA
[g] Department of Radiology, Harvard Medical School, Boston, MA 02115, USA
[h] Department of Physics, Harvard University, Cambridge, MA 02138, USA
[i] Russian Academy of Sciences, Leninskiy Prospekt 14, 119991 Moscow, Russia
[j] Department of Chemistry, Integrative Biosciences (Ibio), Wayne State University, Karmanos Cancer Institute (KCI), Detroit, MI, 48202, United States
[k] Sir Peter Mansfield Imaging Centre, School of Physics & Astronomy, University of Nottingham, Nottingham, NG7 2RD, UK

ARTICLE INFO

Article history:
Received 31 December 2019
Accepted 7 January 2020
Available online 16 January 2020

Keywords:
Xenon
SEOP
Lung imaging
Hyperpolarised

ABSTRACT

Spin-exchange optical pumping (SEOP) can enhance the NMR sensitivity of noble gases by up to five orders of magnitude at Tesla-strength magnetic fields. SEOP-generated hyperpolarised (HP) ^{129}Xe is a promising contrast agent for lung imaging but an ongoing barrier to widespread clinical usage has been economical production of sufficient quantities with high ^{129}Xe polarisation. Here, the 'standard model' of SEOP, which was previously used in the optimisation of continuous-flow ^{129}Xe polarisers, is modified for validation against two Xe-rich stopped-flow SEOP datasets. We use this model to examine ways to increase HP Xe production efficiency in stopped-flow ^{129}Xe polarisers and provide further insight into the underlying physics of Xe-rich stopped-flow SEOP at high laser fluxes.

1. Introduction

Spin-exchange optical pumping (SEOP), a method of nuclear spin hyperpolarisation [1,2], can be used to enhance the NMR detection sensitivity of noble gases by up to five orders of magnitude at Tesla-strength magnetic fields [3]. Noble gas isotopes polarised by SEOP include ^{21}Ne, [4] ^{83}Kr [5], ^{131}Xe [6], ^{131m}Xe [7], ^{3}He [8], and ^{129}Xe [1–3]. For biomedical applications, hyperpolarised (HP) ^{129}Xe has emerged as a versatile and viable agent, with current MR based biomedical applications and drivers for the technology including lung imaging [9–16], brain imaging [17–19], the study of brown adipose tissue (BAT) [20], and various functionalised host-guest biosensors [21–32], a number of which are currently reaching a high level of maturity in *in vitro* studies of disease [33,34]. Each of these applications take advantage of various properties of ^{129}Xe including its moderate tissue solubility, exquisite chemical shift sensitivity, avidity for binding to proteins and other molecular hosts, its lipophilic tendencies, non-toxic nature, and sufficiently long *in vivo* T_1 relaxation times that permit delivery to distal tissues–all of which have been discussed previously in a number of reviews [35–40].

Production of HP ^{129}Xe by SEOP begins with the optical pumping of alkali metal (typically Rb) valence electrons using circularly polarised light resonant at the D_1 transition. This process quickly leads to a highly polarised Rb electronic ground state that subsequently polarises the ^{129}Xe nuclear spins through a combination of binary and molecular van der Waals (vdW) collisions wherein spin-exchange occurs, mediated by the Fermi contact hyperfine interaction [41,35,3,42,2].

A major barrier to generating high ^{129}Xe polarisations at high concentrations – of particular value for lung imaging – is the high

* Corresponding author.
E-mail address: bgoodson@chem.siu.edu (B.M. Goodson).
[1] Present address: Department of Nuclear Medicine, Klinikum rechts der Isar, The Technical University of Munich (TUM), Munich, Germany.
[2] Present address: The Ohio State University College of Medicine, Columbus, OH, USA.

https://doi.org/10.1016/j.jmr.2020.106686
1090-7807/

rate of Xe-induced Rb spin order destruction (hereafter referred to as spin destruction (SD)) that scales with Xe density [3]. Continuous-flow (CF) polarisers – the original method for producing large (~liter*atm) quantities of polarised ^{129}Xe [43] – usually approach this issue by polarising at low Xe concentrations (i.e. typically 1 or 2% of the gas mix, with helium forming the dominant part because of its low SD rate [44,43,45–48]. See Ref [49] for a notable exception), using cryogenic separation methods to increase the HP Xe concentration post-SEOP [43]. Historically however, this method has not produced the ^{129}Xe polarisations predicted by theory e.g. with Norquay et al. producing 12% polarisation against a predicted 24% during an optimisation study [45], among other cases [43,47].

In 2014, this discrepancy between theory and experiment in the CF approach was addressed by Freeman et al. [46] after they hypothesized that the continuous flow of a cold noble gas over molten Rb may inherently promote the formation of deleterious Rb clusters within the optical pumping (OP) cell [46]. The Rb clusters were expected to impact the system by depolarising both the Rb and Xe spins, and by scattering the incident light of the OP laser. Additionally, it was anticipated that the use of high resonant flux at the D_1 transition may accelerate Rb cluster formation [46]. By incorporating Rb clusters into the existing theoretical framework [50,45], the authors were able to more accurately model CF SEOP over a range of OP cell sizes and a range of laser linewidths [46]. Additionally, after modifying the experiment to minimise the formation of the clusters – primarily via a Rb pre-saturator (precedent for which existed with the rationale that it maintains a more stable Rb density [44]) – they were able to substantially improve their production rates and bring P_{Xe} performance in line with the model. While Rb clusters have yet to be detected *in situ* [51], that work provided both compelling evidence for the existence of Rb clusters in CF polarisers, and a pathway through which to improve performance.

Clinical-scale Xe-rich stopped-flow (SF) SEOP, an alternate approach to producing large volumes of HP ^{129}Xe, is now well-established in the literature [52–58], and has been used to produce very high P_{Xe} values (up to 90.9% ± 5.2% [53]) – even at high Xe concentrations i.e. 74% ± 7% at 1000 Torr [55], despite the prevailing high rates of Xe-induced SD. At the cost of having the HP Xe diluted by the presence of buffer gases (which are minimised for Xe-rich gas mixtures), the ability to avoid cryo-collection makes SEOP devices simpler and easier to automate, and reduces the concern of ^{129}Xe hyperpolarisation depletion during storage or phase changes. SF SEOP has been modelled previously (e.g., [59,60]), but rarely in the Xe-rich regime [61,62], particularly in the context of optical pumping with high resonant flux. Here, two sets of simulations of SF SEOP – hereafter referred to as 'Sim1' and 'Sim2' – are presented and compared to two literature datasets. Sim1 [61,62] is a 2D (z,r) Mathematica-based approach that was originally conducted to aid interpretation of our collaboration's initial SF results [52] (dubbed 'Dataset1' in this contribution). Sim2 is a 1D (z) Python-based approach that draws on the theoretical framework used in the optimisation of the CF ^{129}Xe polarisers described above [45,46]. In the present work, both Sim1 and Sim2 are used to model Dataset1 [52]; Sim2 alone is used to model 'Dataset2', which are the experimental results of a multi-parameter optimisation study using our consortium's 'XeUS' SF polariser [56].

Sim1 and Sim2 are found to provide excellent qualitative and quantitative descriptions of Xe-rich SF SEOP, including the inverse relationship between the optimal (externally measured) cell temperature for SEOP (T_{opt}) and Xe density ([Xe]) that characterises this regime – an effect that was previously exploited to achieve high polarisations [52,56]. Furthermore, Sim2 results revealed that under certain conditions the simulations trended towards a 'universally optimal' amount of laser absorption at P_{max}, and these results may i) help provide both an explanation for the observed interplay of laser linewidth, T_{opt}, and [Xe], in the context of optimising the photon-to-[Rb] ratio (discussed below), and ii) provide a new way to quickly optimise SF polarisers. Finally, the validated Sim2 is used to investigate how to modify the design and operation of clinical-scale SF polarisers to further improve their performance. The simulations considered cell temperature, cell geometry, laser linewidth, laser power, gas mixture, and gas pressure, with results including that reduction of laser linewidth (and therefore increasing resonant intensity) improves P_{Xe} disproportionately more at higher [Xe].

2. Theory

A theoretical framework for SEOP by Wagshul and Chupp [50] was updated and used as the basis for modelling of CF polarisers by Norquay et al. in 2013 [45], with Freeman et al. introducing the Rb cluster terms in 2014 [46]. Sim2 is based largely on these models, and as such the pertinent aspects are recounted here. Sim1 drew on earlier literature sources, detailed at the end of the theory section.

2.1. Optical Pumping

The optical pumping rate, γ_{OP}, is dependent on the overlap of the Rb absorption cross section, σ_s, and the photon flux of the laser, Φ, as it traverses the length, z, of the optical pumping cell:

$$\gamma_{OP}(z,\nu) = \int \Phi(z,\nu)\sigma_s(\nu)d\nu. \tag{1}$$

σ_s is commonly approximated with a Lorentzian line-shape[3] that varies as a function of frequency, ν, in the following way:

$$\sigma_s(\nu) = \sigma_0 \frac{\Gamma_{Rb}^2}{4(\nu-\nu_{D_1})^2+\Gamma_{Rb}^2}, \tag{2}$$

where Γ_{Rb} is the FWHM of the pressure-broadened Rb cross section which has an (air-referenced) centre frequency ν_{D_1} of c/794.77 nm [64]. The peak amplitude σ_0 is given by:

$$\sigma_0 = \frac{2r_e c f}{\Gamma_{Rb}}, \tag{3}$$

where r_e is the classical electron radius, c is the speed of light, and f is the oscillator strength of the D_1 transition, which has been shown to have a value of 0.337 [65,45].

Xe, N_2, and He – gases often present in SEOP OP cells – pressure-broaden the Rb transition at different rates. These values were measured by Romalis et al. to be 18.9, 17.8, and 18 GHz/amagat for ^{129}Xe, N_2, and He, respectively [63]. The total broadening in the presence of all three gases is thus:

$$\Gamma_{Rb}[\text{GHz}] = 18.9[\text{Xe}] + 17.8[\text{N}_2] + 18.0[\text{He}], \tag{4}$$

where square brackets indicate the density of the gas in amagats.

The spectral profile of the laser was approximated with a Gaussian line-shape and varies with frequency according to:

$$I(\nu) = I_0 e^{-\left(\frac{\nu-\nu_{Las}}{\Gamma_{Las}}\right)^2}, \tag{5}$$

where ν_{Las} is the centre frequency of the laser, Γ_{Las} is the standard deviation of the Gaussian laser spectrum,[4] and I_0 is the beam intensity at the cell front given by:

[3] Out of simplicity, deviations from a Lorentzian line-shape of the Rb absorption profile [63] were not included in the present simulations.

[4] conversion of FWHM to standard deviation was performed using: $\Gamma_{Las} = \frac{Las_{FWHM}}{[2\sqrt{2\ln(2)}]}$

$$I_0 = \frac{P}{Ah\sqrt{\pi}\Gamma_{\mathrm{Las}} v_{\mathrm{Las}}}, \tag{6}$$

where h is the Planck constant, P is the power, and A is the area of laser illumination which is assumed here to be equal to the cross sectional area of the OP cell. The photon flux Φ through the OP cell has been estimated as [45]:

$$\Phi(z,\nu) = I(\nu)e^{[-\lambda^{-1}(z,\nu)z]}, \tag{7}$$

where λ^{-1} is the position-dependent absorption length. For a cell illuminated by a circularly polarised beam of positive helicity σ^+, λ^{-1} is defined as [50]:

$$\lambda^{-1}(z,\nu) = \sigma_s(\nu)[\mathrm{Rb}](1 - P_{\mathrm{Rb}}(z)), \tag{8}$$

in which [Rb] is the Rb vapour number density in cm^{-3} and $P_{\mathrm{Rb}}(z)$ is the position dependent Rb polarisation. [Rb] in this case was modelled as [66]:

$$[\mathrm{Rb}] = \frac{10^{26.180-(\frac{4040}{T})}}{T}, \tag{9}$$

where T is the temperature in Kelvin.

2.2. Rubidium Polarisation

The Rb polarisation, $P_{\mathrm{Rb}}(z)$, is a function of the optical pumping rate, $\gamma_{\mathrm{OP}}(z,\nu)$, and the Rb spin destruction Γ_{SD}:

$$P_{\mathrm{Rb}}(z) = \frac{\gamma_{\mathrm{OP}}(z,\nu)}{\gamma_{\mathrm{OP}}(z,\nu) + \Gamma_{\mathrm{SD}}}. \tag{10}$$

Away from the walls of the OP cell, Γ_{SD} can occur by two mechanisms: (1) binary collisions with atoms or (2) via the formation of short-lived Rb-Xe vdW molecules. The binary term is:

$$\Gamma_{\mathrm{SD}}^{\mathrm{BC}} = \sum_i [\mathrm{G_i}]\kappa_{\mathrm{SD}}^{\mathrm{Rb-i}}, \tag{11}$$

where $\kappa_{\mathrm{SD}}^{\mathrm{Rb-i}}$ is the Rb SD cross section for Rb binary collisions with each of the gas atoms present in the cell, and $[\mathrm{G_i}]$ is the atomic number density of each gas. Cross section values used in each simulation can be found in Table 1.

The Rb SD rate due to vdW Rb-Xe molecules has been estimated as [45][5]:

$$\Gamma_{\mathrm{SD}}^{\mathrm{vdW}} = \left(\frac{66183}{1 + 0.92\frac{[\mathrm{N_2}]}{[\mathrm{Xe}]} + 0.31\frac{[\mathrm{He}]}{[\mathrm{Xe}]}}\right)\left(\frac{T}{423}\right)^{-2.5} \tag{12}$$

where square brackets indicate gas number density in m^{-3}. Gathering expressions (11) and (12), the total Rb SD is then:

$$\Gamma_{\mathrm{SD}} = \Gamma_{\mathrm{SD}}^{\mathrm{BC}} + \Gamma_{\mathrm{SD}}^{\mathrm{vdW}}. \tag{13}$$

2.3. Xenon Polarisation

The Rb-Xe spin-exchange (SE) rate, γ_{SE}, is the sum of binary and vdW terms, and is given by the following expression [45,46]:

$$\gamma_{\mathrm{SE}} = \gamma_{\mathrm{SE}}^{\mathrm{vdW}} + \gamma_{\mathrm{SE}}^{\mathrm{BC}} = \left(\frac{1}{\sum_i\left(\frac{[\mathrm{G_i}]}{\xi_i}\right)} + \kappa_{\mathrm{SE}}^{\mathrm{Rb-Xe}}\right)[\mathrm{Rb}] \tag{14}$$

$$= (\kappa_{\mathrm{SE}}^{\mathrm{vdW}} + \kappa_{\mathrm{SE}}^{\mathrm{BC}})[\mathrm{Rb}], \tag{15}$$

[5] based on works by Ruset [72] and Nelson et al. [71]

Table 1
Gas-specific binary SD rates as used in Sim1 and Sim2. Units are $\mathrm{cm}^3\ \mathrm{s}^{-1}$.

Cross section	Sim1 value	Sim2 value
$\kappa_{\mathrm{SD}}^{\mathrm{Rb-Rb}}$	–	4.2×10^{-13} [67]
$\kappa_{\mathrm{SD}}^{\mathrm{Rb-He}}$	–	$3.45 \times 10^{-19}(T/298\ \mathrm{K})^{4.26}$ [67]
$\kappa_{\mathrm{SD}}^{\mathrm{Rb-N_2}}$	9.4×10^{-18} [68]	$3.44 \times 10^{-18}(T/298\ \mathrm{K})^{3}$ [69]
$\kappa_{\mathrm{SD}}^{\mathrm{Rb-Xe}}$	5.2×10^{-15} [70]	$6.02 \times 10^{-15}(T/298\ \mathrm{K})^{1.17}$ [71]

where ξ_i is the vdW rate for each gas atom, with number density again given by $[\mathrm{G_i}]$. The vdW rates are in Table 2. $\kappa_{\mathrm{SE}}^{\mathrm{BC}}$ is the binary collision SE cross section and has been reported to be $2.17 \times 10^{-16}\mathrm{cm}^3\mathrm{s}^{-1}$ [75,45].

In a CF SEOP polariser, the nuclear spin polarisation of ^{129}Xe generated through SE with polarised Rb atoms after a given residence time t_{res} is [43]:

$$P_{\mathrm{Xe}}(t_{\mathrm{res}}) = \frac{\gamma_{\mathrm{SE}}}{\gamma_{\mathrm{SE}} + \Gamma}\langle P_{\mathrm{Rb}}\rangle(1 - \exp^{-(\gamma_{\mathrm{SE}}+\Gamma)t_{\mathrm{res}}}), \tag{16}$$

where t_{res} is the average amount of time Xe atoms spend in the OP cell as they flow from the gas cylinder to the cold finger, Γ is the ^{129}Xe SD rate, and $\langle P_{\mathrm{Rb}}\rangle$ is the spatially averaged Rb polarisation within the OP cell. In most CF SEOP setups, Γ is dominated by wall relaxation and equal to $\frac{1}{T_1}$, therefore experimentally measured in-cell T_1 values can be used in the simulations to calculate Γ.

In SF SEOP, the SEOP gas mixture is held static within the OP cell, therefore t_{res} becomes the total OP time t:

$$P_{\mathrm{Xe}}(t) = \frac{\gamma_{\mathrm{SE}}}{\gamma_{\mathrm{SE}} + \Gamma}\langle P_{\mathrm{Rb}}\rangle(1 - \exp^{-(\gamma_{\mathrm{SE}}+\Gamma)t}), \tag{17}$$

and the ^{129}Xe nuclear spin polarisation P_{Xe} will reach steady state as t tends to infinity (~1 h in practice). Under this condition the terminal polarisation can be calculated as:

$$\lim_{t\to\infty} P_{\mathrm{Xe}} = \frac{\gamma_{\mathrm{SE}}}{\gamma_{\mathrm{SE}} + \Gamma}\langle P_{\mathrm{Rb}}\rangle. \tag{18}$$

Note that $\gamma_{\mathrm{SE}} + \Gamma$ is equal to–and quoted as–γ_{SEOP} in a number of publications.

2.4. Alternative Equation Forms Used in Sim1

Sim1 is an earlier simulation that used alternative forms for a number of the equations given above and these are detailed here. For the calculation of the D_1 linewidth a lineshift contribution was also considered [63]:

$$\nu_{D_1}[\mathrm{GHz}] = 377107.4 - 8.5[\mathrm{N_2}] - 5.05[\mathrm{Xe}] + 4.3[\mathrm{He}], \tag{19}$$

where the number densities of the gas species are in amagats. Line broadening (cf. Eq. (4)) was calculated as:

$$\Gamma_{\mathrm{Rb}}[\mathrm{GHz}] = 0.04 + 18.9[\mathrm{Xe}] + 17.8[\mathrm{N_2}] + 18.0[\mathrm{He}]. \tag{20}$$

[Rb] (cf. Eq. (9)) was calculated via:

$$P_V[\mathrm{Torr}] = 10^{(7.193-\frac{4040}{T})}, \tag{21}$$

Table 2
Gas-specific vdW rates (used only in Sim2).

Atomic species	vdW rate
ξ_{Xe}	5230 s^{-1} [73]
ξ_{N_2}	5700 s^{-1} [74]
ξ_{He}	17000 s^{-1} [43]

with T given in Kelvin and P_V standing for Rb vapour pressure. A comparison plot of Eqs. (9) and (21) is available in the ESI. Rb SD (cf. Eqs. (12) and (13)) was determined without the vdW contribution:

$$\Gamma_{SD} = \kappa_{SD}^{Rb-Xe}[Xe] + \kappa_{SD}^{Rb-N_2}[N_2], \tag{22}$$

using temperature independent binary cross section values of $\kappa_{SD}^{Rb-Xe} = 5.2 \times 10^{-15}$ cm^{3}s^{-1} and $\kappa_{SD}^{Rb-N_2} = 9.4 \times 10^{-18}$ cm^{3}s^{-1}, introduced by Bouchiat et al. and Wagshul et al. respectively [70,68].

The SE rate equation (cf. Eq. (14)) took the form of that given by Cates et al. [73,62]:

$$\gamma_{SE} = \left(\langle\sigma v\rangle + \frac{\gamma_M \zeta}{[Xe](1+br)}\right)[Rb], \tag{23}$$

where $\langle\sigma v\rangle = 3.7 \times 10^{-16}$ cm^{3}s^{-1} is the velocity-averaged binary SE cross section, $\gamma_M = 2.94 \times 10^4$ s^{-1} is an experimentally determined constant, $\zeta = 0.1791$ is a value that corresponds to Rb isotope distribution, and $br = 0.275[N_2]/[Xe]$ is a correction factor to account for the differential capacity of N_2 to facilitate formation and break-up of vdW complexes compared to Xe [73].

3. Methods

3.1. Dataset1

To collect Dataset1 [52], ^{129}Xe NMR signal intensity was measured as a function of external cell temperature (T_{cell}) and [Xe] using low-field *in situ* NMR spectroscopy. [Xe] ranged from 50 to 1400 Torr. Gas mixes were backfilled with N_2 to 2000 Torr total pressure at loading and contained in a 1" diameter cylindrical 'Rosen' style OP cell [60] with 75 cc inner cell volume. The B_0-field (32 G) was generated using a Helmholtz coil pair of 22" inner diameter and a Magritek Aurora NMR spectrometer was used for low-field NMR (^{129}Xe frequency: 37.5 kHz).

OP was performed using a TEC-cooled prototype 'Comet' (Newport/Spectra-Physics) fixed-frequency laser diode array (LDA). [76] Output at the OP cell was ~29 W with a spectral linewidth of 0.27 nm centred at 794.66 nm. The laser was specifically driven to have a 'blue-side' spectral offset from the Rb D_1 line to achieve maximum P_{Xe} under those conditions [76]. The LDA was fibre-coupled to the OP cell and a binocular circular polariser box (Coherent) which yielded a 85/15 straight/angled beam ratio was used to circularly polarise the light. A 2" mirror was present behind the cell to retro-reflect excess transmitted laser light back into the OP cell. This practice was found to provide up to a ~29% 'free' increase in P_{Xe} (under nominal conditions; dependent on T_{cell}) [77].

3.2. Dataset2

For Dataset2 [56], ^{129}Xe NMR signal intensity was measured as a function of T_{cell}, [Xe] (275 to 2000 Torr Xe, backfilled with N_2), *and* laser power (100, 125, 142 and 170 W). The laser had a spectral width of 0.3 nm and was centered at 794.8 nm. The measurements were made on board a clinical-scale polariser that has been described previously [56,55]. A Magritek Kea2 low-field NMR spectrometer was used to perform *in situ* NMR polarimetry at 47 kHz. The resulting ^{129}Xe spectra were calibrated against a doped (10 mM $CuSO_4$), thermally polarised water ^{1}H NMR spectrum (acquired with 200,000 averages) that was obtained at the same frequency and in a vessel of the same shape and volume (2"-diameter (500 cc) cell) [56].

Once steady-state ^{129}Xe polarisation curves were obtained, γ_{SEOP} (= $\gamma_{SE} + \Gamma$) values were extracted by fitting the data to Eq. (17). After SEOP, in-cell room-temperature (rt) measurements of T_1 were made by quickly cooling the OP cell down to rt (to minimise the Rb gas-phase concentration), turning off the laser, and acquiring *in situ* NMR spectra while P_{Xe} decayed.

3.3. Sim1

Sim1 simulations were performed using Mathematica (version 8.0.0.0) on a PC. For a given simulation, D_1 spectral width and center were calculated via Eqs. (19) and (20) with a Lorentzian frequency distribution. The simulated laser output was kept centered on the Rb D_1 line with a variable spectral width of 0.25–10 nm. A cylindrical cell was assumed (z, r) and light flux incident on the front of the cell, Φ, was amplitude-modulated in space using a flat 'top-hat' cross-sectional profile and modelled to decay with a Gaussian spatial profile near the cell walls (see Fig. 1). [Rb] was determined solely based on Eq. (21), and was kept homogeneous throughout the cell as no temperature gradients were included in the simulations. Only binary mixtures of Xe and N_2 were considered. [Xe] and [N_2] were determined assuming ideal gases loaded at 293 K.

P_{Rb} at a given position in the cell was determined as an instantaneous function of light flux according to Eq. (10). Light propagation through the cell cannot be calculated directly using Beer's law because polarised Rb atoms [↑] are transparent to circularly polarised light; therefore, light absorption must be determined based on the density of available absorbers, [↓], since the D_1 absorption cross section, σ_s, in Eq. (1) is defined using unpolarised light:

$$[\downarrow] = \frac{[Rb]}{2}(1 - P_{Rb}). \tag{24}$$

Light flux at a given position within the cell was calculated based on a finite number (~200–300) of discrete modified 'Beer's cell layers', where γ_{OP} in the first Beer's cell layer was calculated using Eq. (7) with the integration implemented by Riemann sum using 100–300 steps over ±250 GHz from center (~10 x FWHM), and used to calculate: i) the P_{Rb} value assigned to the first layer as a function of position across the face of the cell, ii) the resulting light attenuation, and iii) [↓] for the next 'Beer's cell layer'. The attenuated input

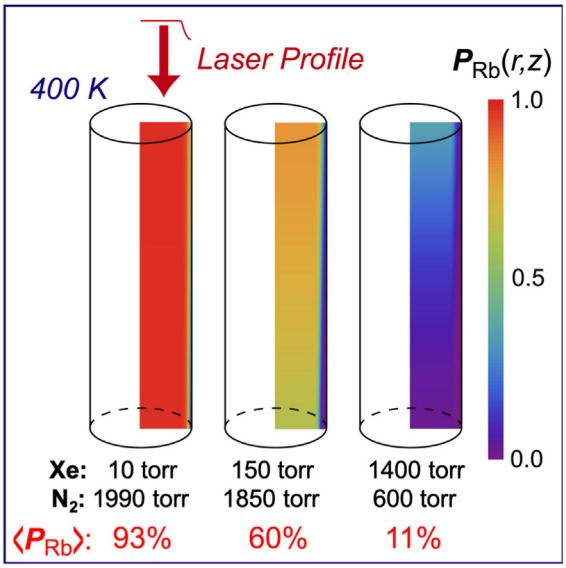

Fig. 1. Three selected simulation plots of P_{Rb} from Sim1: 10, 150, and 1400 Torr Xe with constant T_{cell} and total cell pressure (400 K and 2000 Torr). Each plot was generated with an input radial resolution of 200 with 199 total recursions representing the Rb cell polarisation at any one azimuthal angle. These values were then cylindrically integrated to estimate average Rb polarisation, $\langle P_{Rb} \rangle$, throughout the cell [62].

flux Φ_1 is then applied to the next layer (one step deeper into the cell) and that process is repeated over a total of 100–300 layers in the cell. Finally, the calculated P_{Rb} values can then be volume-averaged across the cell for the quantity $\langle P_{Rb}\rangle$ used to calculate P_{Xe}. Example output of such calculations can be seen in Fig. 1.

3.4. Sim2

Sim2 was written in Python (2.7.13) using the freely available Spyder editor (3.0.2) as contained in the Anaconda distribution. For a given simulation, the Rb D_1 was modelled to experience pressure broadening as given in Eq. (4) and assumed a Lorentzian spectral profile (Eq. (2)). Lineshift was not simulated, and the laser line – modelled with a Gaussian profile (Eq. (2)) – was centred on the D_1 transition at 794.77 nm. Incident light is assumed to be 100% polarised. A 1D cell was assumed (z), equivalent to considering the laser to have no cross-sectional variation in intensity. [Rb] was calculated via Eq. (9) and was modelled as constant throughout the cell. Binary mixtures of Xe and N_2 were considered in the simulation of Dataset1 and Dataset2. He was included in later exploratory simulations of Dataset2. [Xe], [N_2], and [He] were determined assuming ideal gases loaded at 293 K.

Due to the fact that P_{Rb} and γ_{OP} are functions of each other [P_{Rb} depends on γ_{OP} by Eq. (10), and γ_{OP} depends on P_{Rb} by Eqs. (1), (7) and (8)], $\langle P_{Rb}\rangle$ and γ_{OP} were determined using an equilibrium function approach: Eqs. (1), (2), (7), and (8) were combined to give the following integral [in accordance with Eqn. (1)] and solved numerically using the Trapezoid rule over a given frequency range $[\nu_{min}, \nu_{max}]$ for 300 discrete values of z:

$$\gamma_{OP}(z,\nu) = \int_{\nu_{min}}^{\nu_{max}} I_0 e^{-\left(\frac{\nu-\nu_{Las}}{\Gamma_{Las}}\right)^2} e^{(-\lambda^{-1}z)} \sigma_0 \frac{\Gamma_{Rb}^2}{4(\nu-\nu_{D_1})^2+\Gamma_{Rb}^2} d\nu, \qquad (25)$$

where $\nu_{min} = \nu_{Las} - 5\Gamma_{Las}$ and $\nu_{max} = \nu_{Las} + 5\Gamma_{Las}$.

To calculate a cell averaged P_{Rb} value, an initial 'guess' (P_{Rb} = 0) is firstly substituted into Eq. (25) for z = 0. An output value of P_{Rb} is calculated for the given experimental conditions. The new value is then compared to the initial P_{Rb} value (the guess). If the difference between the values is greater than 1×10^{-8}, the equilibrium function condition is not satisfied, and the new P_{Rb} value is fed back into the calculation in place of the previous value and a further new P_{Rb} is calculated. This process continues until the equilibrium condition is satisfied, at which point the value is accepted as the true P_{Rb} value for z = 0. The resulting P_{Rb} is then used as the initial guess for the next z and the process is repeated for the length of the OP cell which is divided into 300 discrete z values. The 300 $P_{Rb}(z)$ points are averaged to obtain the spatially averaged P_{Rb} value, $\langle P_{Rb}\rangle$, as used in the calculation of P_{Xe}.

3.4.1. Exploratory Simulations with Sim2

For the exploratory simulations of Dataset2, modifications to the OP cell geometry, gas mix composition, laser linewidth, and/or total cell pressure were made within Sim2. The modified parameters used for the OP cell geometry (Figs. 9 and 10) and laser linewidth (Figs. 9–11) are shown in Table 3. For simulations including He (Fig. 10), the gas mix was modified such that He constituted 90% of the buffer gas balance that would otherwise be completely N_2. For simulations with a modified geometry, in-cell T_1 relaxation was scaled according to the surface-area to volume (S/V) ratio. For simulations that modulated the total gas pressure (Figs. 9 and 11), the constituent gases were multiplied by the factors: 0.25, 0.5, 1, 2, 10. In some cases, multiple modifications were simulated simultaneously (e.g., a 3" cell, with He, and a 0.015 nm FWHM laser – Fig. 10). Simulations at 0.015 nm were performed due to the recent emergence of lasers with this linewidth at the Rb D_1.

3.5. Phenomena not modelled

Rb cluster terms were not included in Sim1 or Sim2 because the previously calculated higher efficiencies of the SF polarisers do not indicate a loss pattern that could be explained by Rb clusters [54]; furthermore, flow conditions suspected of driving Rb cluster formation [46] are absent in SF polarisers. Other effects not incorporated include: Collision-induced Rb spectral line asymmetries (that have their own dependencies on gas partial pressures and temperatures [63]); choice of alkali metal besides Rb [78,79]; gas motion from either diffusion or convection [59]; any potential effects of laser detuning [80]; or greatly elevated gas temperatures that have been observed via in-situ Raman spectroscopy [81–83].

4. Results and discussion

4.1. Comparison of Sim1 and Sim2 to Dataset1

Fig. 2(a) summarises Dataset1: the results of the SEOP experiments where the Xe-rich SF regime was first probed under high resonant flux conditions [52]. ^{129}Xe NMR signal intensity is plotted as a function of T_{cell} for the gas mixes investigated: 50, 100, 300, 500, 950, 1400 Torr Xe, each backfilled to 2000 Torr with N_2. The maximum signal intensity for each gas mix occurs at a different T_{cell} value, and as [Xe] increases, its respective peak value was observed to shift to lower temperatures. This inverse relationship

Table 3
Key experimental parameters. Entries in Dataset1 marked with an asterisk are those used in the simulations only. Sim1 and Sim2 simulations of Dataset1 and Dataset2 used the entries in the Dataset1 and Dataset2 columns. Parameters for the exploratory simulations of Dataset2 with Sim2 are displayed in the 5 rightmost columns. The 'Linewidth' column shows the values used in simulations in which the pump laser FWHM was modulated. The final four columns show the values used in simulations in which the OP cell diameter or OP cell length was modulated.

	Experimental data		Exploratory Sim2 simulations				
Parameter	Dataset1 [52]	Dataset2 [56]	Laser FWHM Linewidth	D = 3 "	D = 1 "	L = 50 cm	L = 100 cm
Cell radius [cm]	1.27	2.54	2.54	3.81	1.27	2.54	2.54
Cross-sectional area [cm^2]	5.07	20.3	20.3	45.6	5.07	20.3	20.3
Cell length [cm]	15.0	25.0	25.0	25.0	25.0	50.0	100.0
Cell volume [cm^3]	76.0	507	507	1140	127	1010	2030
Surface area [cm^2]	130	440	440	690	209	839	1640
S/V ratio [cm^{-1}]	1.71	0.87	0.87	0.61	1.65	0.83	0.807
In-cell T_1 [hrs]	0.16	2.5	2.5	3.56	3.63	2.62	2.7
(Xe)$\Gamma = \frac{1}{T_1}$ [s^{-1}]	1.66×10^{-3}	1.11×10^{-4}	1.11×10^{-4}	7.8×10^{-5}	7.65×10^{-5}	1.06×10^{-4}	1.03×10^{-4}
Laser power [W]	29	100, 125, 142, 170	100, 125, 142, 170	100, 125, 142, 170	100, 125, 142, 170	100, 125, 142, 170	100, 125, 142, 170
Laser FWHM [nm]	0.25∗, 0.27, 3.0∗, 10.0∗	0.3	0.015, 0.15, 0.3, 10.0	0.015, 0.15, 0.3	0.15, 0.3	0.15, 0.3	0.15, 0.3

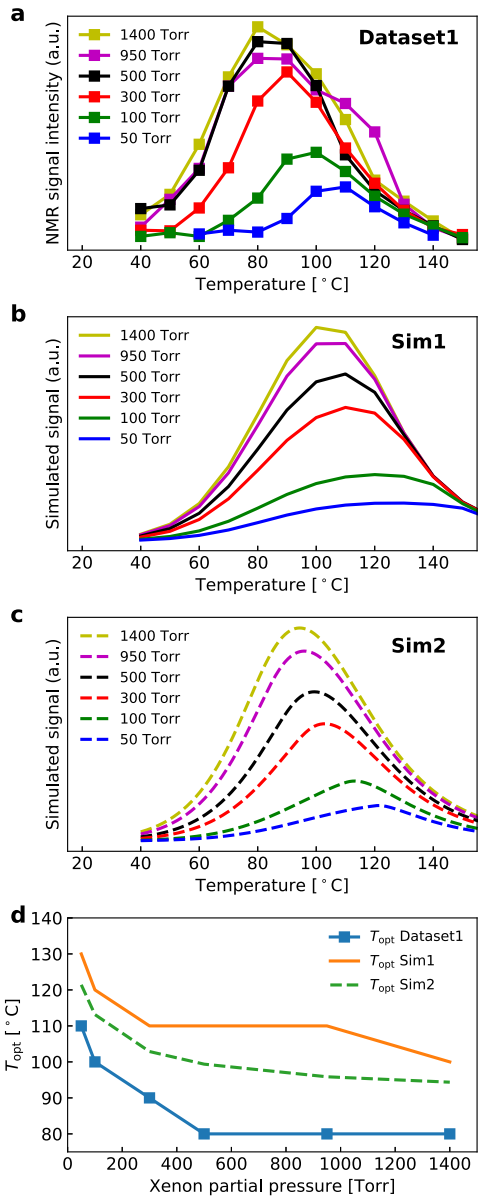

Fig. 2. Dataset1 and corresponding Sim1 and Sim2 simulations. (a) HP ^{129}Xe NMR signal intensity as a function of T_{cell} for 50, 100, 300, 500, 950, and 1400 Torr of Xe, back filled to 2000 Torr with N_2 in a L = 15 cm, r = 1.27 cm OP cell illuminated with a 29 W, 0.27 nm FWHM laser at 794.66 nm. In-cell T_1 = 0.16 h. Sim1 and Sim2 simulation results appear in (b) and (c) respectively. (d) Simulated and experimental optimal temperature, T_{opt}, plotted as a function of [Xe]. Dataset1 in (a) reproduced with permission from reference [52]. Simulations in (b) reproduced from references [62,61]. See Table 3 for further parameters.

can be seen more clearly in Fig. 2 – a plot of optimal temperature, T_{opt}, against [Xe]. Fig. 2(b) and (c) show the results of Sim1 and Sim2, respectively, for these experimental conditions. For Sim1 and Sim2, the product of the P_{Xe} and [Xe] is plotted, proportional to the NMR signal intensity, as is shown for Dataset1 in (a).

Sim1 and Sim2 quantitatively recapture much of the inverse relationship exhibited by T_{opt} and [Xe] in Dataset1, exhibiting only a vertical offset from Dataset1 (of 30 °C at its worst) that is likely explained by a difference between the true gas temperature within the OP cell and that measured experimentally using a thermocouple at the cell exterior. The reality is that within the cell a range of temperatures exist – extreme temperatures under some conditions [58], driving convective or turbulent flow patterns that have been observed with Raman spectroscopy [81]. But the agreement shown here indicates that even a simplistic 1D model is able to provide an adequate description of the prevailing SEOP physics under the high-[Xe], high-photon-flux SF regime when averaging over the entire cell. As an aside, there have been instances where P_{Xe} has been greater at higher [Xe] than at lower [Xe] [76,52]. This experimental result was not reproduced by either simulation.

The overall inverse temperature trend can be explained in terms of the Xe-induced Rb SD rate which is mediated by the Xe-Rb spin-rotation interaction: Higher [Xe] results in greater rates of Xe-induced Rb spin destruction, which in turn increases opacity in the OP cell. By reducing the OP cell temperature at higher [Xe], [Rb] is reduced, leading to an increase in photon flux throughout the cell and thus increased P_{Rb} and P_{Xe} values, albeit at the expense of γ_{SEOP}. In the limit where the in-cell ^{129}Xe T_1 is long (approaching infinity), optimising the 'photon-to-[Rb] ratio' is central to achieving a high P_{Xe} value. In separate simulations with Sim1, the same trends with only a slight temperature shift were borne out when the 3-body contributions were removed, further emphasising the central role of the photon-to-[Rb] ratio. In experiments, the effect was also found to be independent from [N_2] and the xenon nuclear spin destruction rate [58].

4.2. Investigations of laser linewidth effects using Sim1 and Sim2

By considering P_{Xe} as a function of laser linewidth, the results from the Sim1 and Sim2 simulations in Figs. 3 and 4 provide insight into how Xe-rich mixes can perform so well in spite of the high accompanying rate of Rb spin destruction, and provide

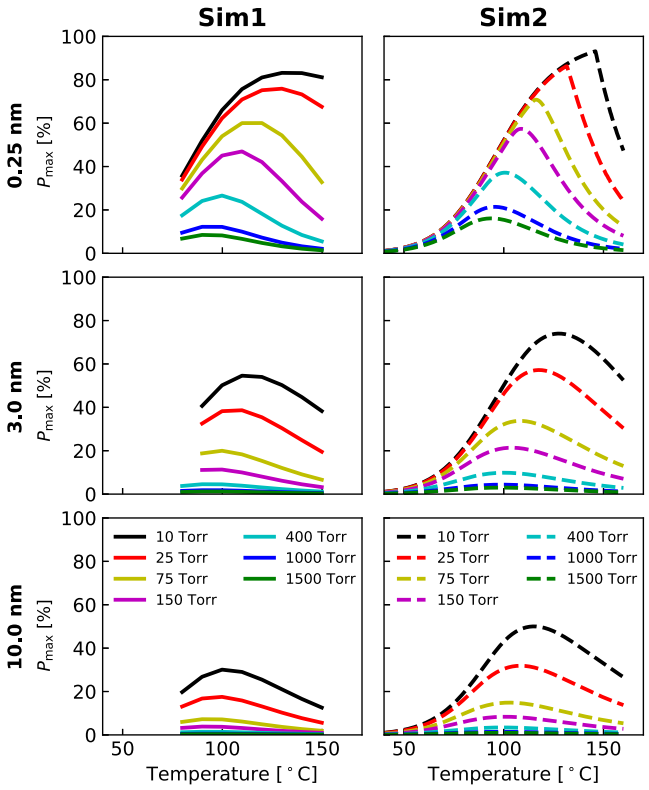

Fig. 3. Simulations of SF SEOP as a function of OP laser linewidth (0.25, 3, 10 nm FWHM) for seven Xe:N_2 gas mixes: 10, 25, 75, 150, 400, 1000 and 1500 Torr Xe, back-filled to 2000 Torr with N_2 in a L = 15 cm, r = 1.27 cm OP cell illuminated with a 29 W laser. Simulated laser and D_1 spectral lines were aligned in both simulations. In-cell T_1 = 0.16 h. As the laser linewidth increases, P_{max} for a given gas mix drops, and the distribution (particularly its peak, T_{opt}) becomes less sensitive to temperature. T_{opt} decreases with increasing [Xe], and the polarisation increases with narrowing linewidth at a greater relative rate for higher [Xe] mixes.

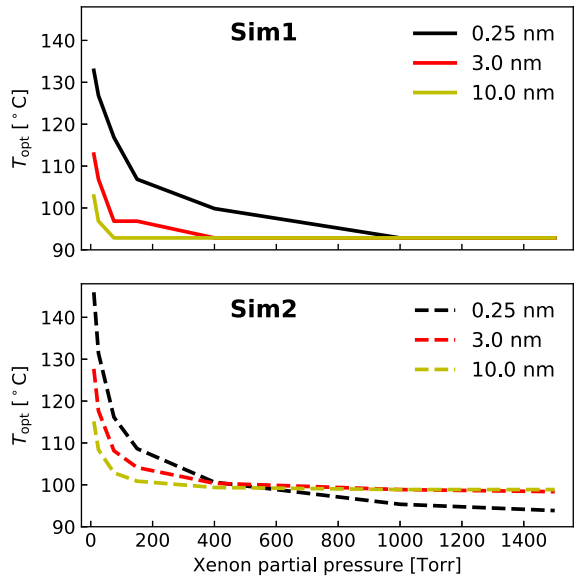

Fig. 4. Comparison of T_{opt} behaviour for Sim1 and Sim2 as a function of laser linewidth (cf. Fig. 2(d)) for seven Xe:N_2 gas mixes: 10, 25, 75, 150, 400, 1000 and 1500 Torr Xe, back-filled to 2000 Torr with N_2 in a L = 15 cm, r = 1.27 cm OP cell illuminated with a 29 W laser. Simulated laser and D_1 spectral lines were aligned in both simulations. In-cell T_1 = 0.16 h. In both Sim1 and Sim2, T_{opt} decreases with increasing [Xe], and as linewidth increases, P_{max} becomes less sensitive to T. Sim1 results reproduced from reference [62].

further support to the importance of optimizing the 'photon-to-[Rb]' ratio. Both simulations indicate that as the spectral linewidth of the laser is increased (while keeping total incident laser power constant), both P_{Xe} *and* T_{opt} decrease; P_{Xe} also becomes less sensitive to T, as manifested by the broadening distributions. Looking at it the other way, as P_{Xe} becomes more sensitive to T as the laser linewidth is reduced, richer [Xe] mixes enjoy a disproportionally greater gain in signal intensity. The effect at the highest Xe densities is striking: note particularly the 1500 Torr mix, which sees P_{Xe} increase from ~1% to almost 10% and 20% in Sim1 and Sim2 respectively as the spectral linewidth is reduced from 10 nm to 0.25 nm FWHM. This disproportionally greater gain in P_{Xe} at higher [Xe] is because there is more potential at higher [Xe] to recover P_{Xe} by reducing T (reducing the Rb density), countering the Rb-SD induced optical opacity that causes P_{Rb} – and consequently P_{Xe} – to plummet.

The P_{max} values of the lowest two Sim2 [Xe] curves peak sharply in the 0.25 nm FWHM simulations. Likely origins for this 'effect' include (i) the 'simplistic' 1D nature of the model combined with (ii) performing the simulations at the 'extreme' conditions of very narrow laser spectral widths, and with (iii) the assumption of 100% polarised light; under these conditions, we are closer to the limit of effectively zero Xe-induced Rb spin destruction, so the effect of narrowing the laser linewidth (and coupling increasingly to the Rb D_1 and the temperature dependent Rb vapour density) dominates the behaviour of both P_{Rb} and P_{Xe}. Indeed, there is a sharp transition from complete in-cell optical transparency to partial transparency as T_{cell} is increased, which manifests here as a sharpening spike in the P_{Xe} curves in the upper right hand corner of Fig. 3. This effect is apparent in Sim2 (a 1D model) and not in Sim1 (a 2D model), because Sim1 also includes a polarised-light attenuation function at the walls, reducing susceptibility to this effect under such extreme conditions. Implementing a lower incident light polarisation in Sim2 (e.g. ~95%) correspondingly softens the P_{Xe} curves. (Similar behaviour is apparent later in some Sim2 simulations of Dataset2 conditions with extreme laser narrowing to 0.015 nm FWHM; cf. Fig. 9).

Fig. 4 summarises the T_{opt} behaviour across these simulated data sets. Although normalised differently, both sets of simulations show increased sensitivity to temperature at narrower linewidths. This result likely explains why – before such narrow, high-powered lasers were used for SEOP – the temperature-sensitive nature of P_{Xe} as a function of [Xe] (which in turn led to HP Xe preparations with high P_{Xe} at high [Xe] by exploiting T_{opt}) [52,56] had not been previously noticed. Indeed, studies using broadband lasers have tended to report little or no dependence of T_{opt} on [Xe] [78].

4.3. Comparison of Sim2 to Dataset2

Fig. 5 summarises Dastaset2, the results of the XeUS multidimensional study [56]. In these experiments, P_{Xe} and γ_{SEOP} were measured as a function of T_{cell}, incident laser power, and [Xe]. For each gas mix, the maximum measured values are plotted as colour contour maps in panels (c), (e), (g), (i), and (k) for P_{Xe} and panels (d), (f), (h), (j), and (l) for γ_{SEOP}. Fig. 5(a) shows a cross-section of the P_{Xe} and γ_{SEOP} data from panel (g) as an example – the 1000 Torr mix at ~100 W of lasing power – and panel (b) shows the optimal values of P_{Xe} and γ_{SEOP} for each gas mix. P_{Xe} and γ_{SEOP} values were obtained from fits to a form of Eq. (17).

As discussed in the original publication [56], the data exhibit several trends, most of which are borne out in the Sim2 results in Fig. 6. For instance, when considering the γ_{SEOP} data (panels (d), (f), (h), (j) and (l)) it can be seen that increasing T_{cell} gives rise to an expected exponential increase in γ_{SEOP}, reflecting the dependence on [Rb] (by Eqs. (14) and (23)) which increases exponentially with T (Eq. (9)). However, hints of laser-induced heating are evident in the experimental data that are absent in Sim2. A pure dependence on [Rb] would mean that the colour contours would run purely vertically – as is the case in the simulations – but in Dataset2, as the laser power is increased, γ_{SEOP} begins to elevate at lower T_{cell}. The relative contributions of γ_{SE}^{BC} & γ_{SE}^{vdW} to γ_{SEOP} predicted by Sim2 across the whole of Dataset2 can be seen in the ESI. γ_{SE}^{BC} provides the greater contribution in every case under the conditions studied.

P_{Xe} follows a different trend throughout. Taking panel (a) in both Figs. 5 and 6 as an example, it can be seen that as T_{cell} is increased, P_{Xe} initially grows until P_{max} is reached, as given by Eq. (18). $\langle P_{Rb} \rangle$ here is given by Eq. (10). These eqns show that P_{Xe} approaches $\langle P_{Rb} \rangle$ when γ_{SE} is much greater than Γ, which occurs at higher temperatures (by Eq. (14)); however, this also leads to a higher density of absorbers, which reduces photon flux through the rear regions of the OP cell, lowering γ_{OP} across the cell and thus $\langle P_{Rb} \rangle$, placing a limit on the achievable xenon polarisation (P_{max}). In other words, P_{max} initially grows with increasing T as more Rb is vaporised, but once [Rb] becomes too high, overall $\langle P_{Rb} \rangle$ decreases, resulting in the lower P_{max} values at higher T_{cell} values. (This interplay between P_{max}, $\langle P_{Rb} \rangle$, and light absorption is shown in Fig. 8.).

There are regions of no data in Dataset2 (Fig. 5). This absence is because: i) either γ_{SEOP} was excessively low (resulting in impractically long experiments for the prevailing time constraints), or ii) it was not possible to measure P_{max} without inducing 'Rb runaway', which occurs when undissipated heat from laser absorption or cell heating rapidly compounds the amount of Rb in the vapour phase over a short time [47,80,84]; the uncontrolled growth of [Rb] results in decreasing P_{Rb} in more poorly illuminated regions of the OP cell and hence more laser absorption and heat dissipation from the gas into the inner surface of the cell (and Rb pools) in a self-reinforcing pattern. Rb runaway is more common at higher [Xe] because the rates of Xe-induced Rb spin destruction are higher and (likely) because the thermal conductivity of the gas mixture is lower due to the increased presence of Xe.

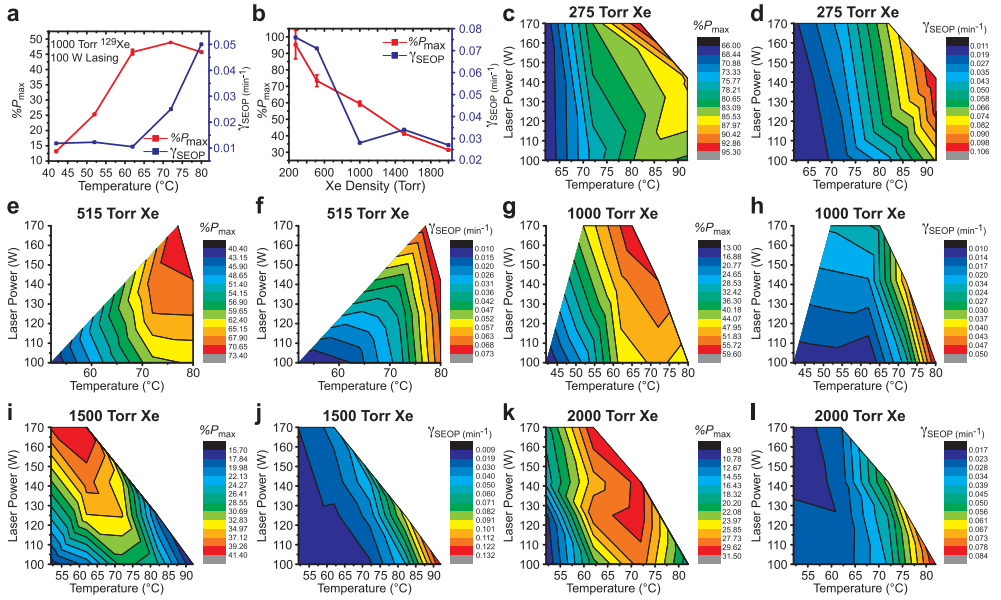

Fig. 5. Dataset2: results of the XeUS multi-parameter study. P_{Xe} and γ_{SEOP} were measured as a function of T_{cell}, incident laser power, and [Xe] for five Xe:N_2 gas mixtures contained within a L = 25 cm, r = 2.54 cm OP cell. The maximum values for P_{Xe} and γ_{SEOP} for each gas mix at each temperature and laser power are plotted in colour contour maps (c), (e), (g), (i), and (k) for P_{Xe} and (d), (f), (h), (j), and (l) for γ_{SEOP}. P_{Xe} and γ_{SEOP} were determined from fits to a form of Eq. (17). (a) shows a cross-section of panel (g): P_{Xe} and γ_{SEOP} for the 1000 Torr mix at 100 W. (b) shows $P_{max} - P_{Xe}$ at the optimal temperature T_{opt} for each gas mix – and the corresponding γ_{SEOP} values. Reprinted with permission from Ref. [56] Copyright (2014) American Chemical Society.

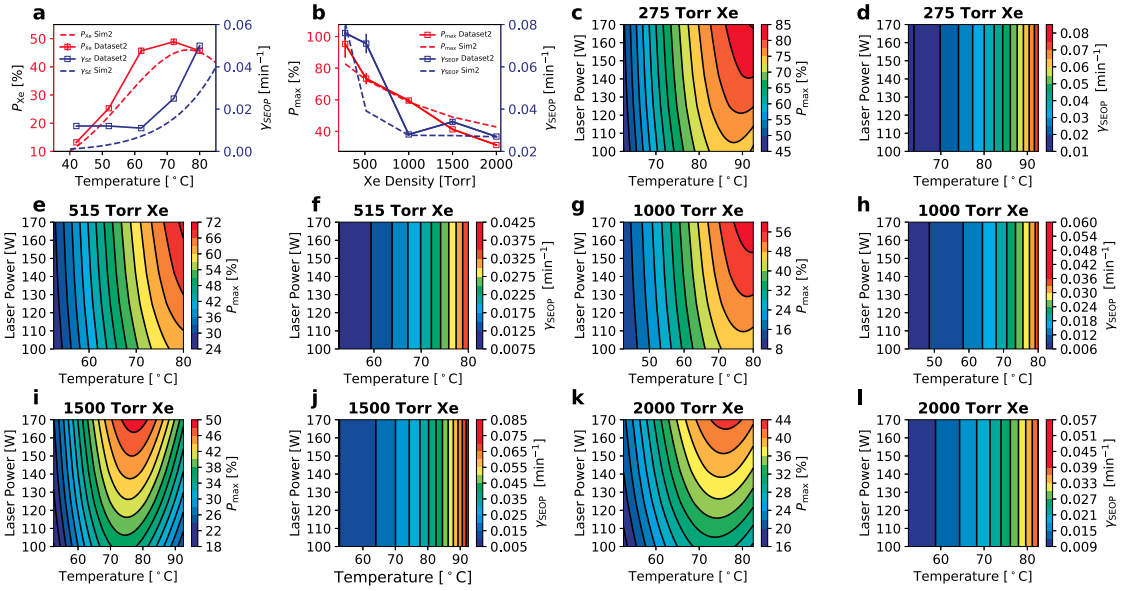

Fig. 6. Sim2 simulations of Dataset2 (c.f. Fig. 5). P_{Xe} and γ_{SEOP} simulated as a function of T_{cell}, incident laser power, and [Xe] for five Xe:N_2 gas mixtures contained within a L = 25 cm, r = 2.54 cm OP cell. Maximum values for P_{Xe} and γ_{SEOP} for each gas mix at each temperature and laser power are plotted in colour contour maps (c), (e), (g), (i), and (k) for P_{Xe} and (d), (f), (h), (j), and (l) for γ_{SEOP}. (a) shows a cross-section of panel (g): simulations P_{Xe} and γ_{SEOP} for the 1000 Torr gas mix at P = 100 W. Simulations (dashed lines) are plotted with the corresponding experimental data (solid lines, square markers). (b) shows simulation derived (dashed lines) and experimentally measured (solid lines, square markers) $P_{max} - P_{Xe}$ at the optimal temperature T_{opt} for each gas mix – as well as the corresponding γ_{SEOP} values. Further parameters are summarised in Table 3.

Panel (b) of Fig. 6 shows the optimal P_{Xe} values from Dataset2 as a function of [Xe], plotted for comparison against the corresponding Sim2 predictions. Overall, good qualitative and quantitative agreement is observed: in particular, Sim2 predicts the P_{max} of the 515 Torr and 1000 Torr mixtures to within 1%. The model underestimates P_{max} at 275 Torr, but the experimental error is large. At higher [Xe] the experimental data are lower than that predicted by Sim2, and this discrepancy may be due to thermal effects that are not considered by the model that worsen at higher [Xe] for at least two possible reasons: i) increased rates of non-radiative de-excitation of the Rb via the resulting heat-generating Rb-N_2 collisions (due to greater Xe-induced Rb-SD at higher [Xe]), and ii) the bulk thermal conductivity reduces because more-thermally-conductive N_2 is replaced by Xe.

As [Xe] is increased from 275 Torr to 2000 Torr, the same inverse relationship with T_{opt} present in Dataset1 is again apparent: T_{opt} decreases from 82 °C to 62 °C (a drop of 20 °C) in Dataset2, and 93.8 °C to 76.3 °C (a drop of 17.5 °C) in Sim2 (Fig. 7). Both Sim2 and Dataset2 exhibited higher Xe polarisations with increasing laser power throughout the tested range. Thus, the use

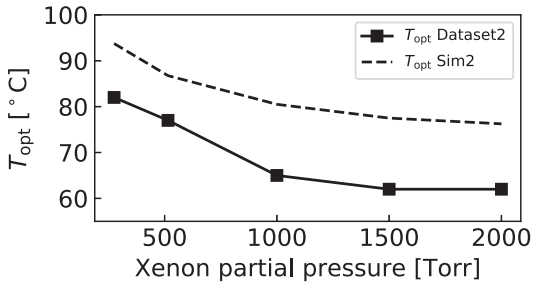

Fig. 7. T_{opt} as a function of [Xe] for Dataset2 (solid lines, square markers) and Sim2 (dashed lines), c.f. Figs. 5(b) and 6(b). As with Dataset1 (Fig. 2(d)), the temperature at which P_{max} occurs for a given gas mix (T_{opt}) decreases with increasing [Xe]. The offset is likely explained by a difference between the true gas temperature within the OP cell and that measured experimentally using a thermocouple at the cell exterior. Experimental data from the SI of Ref. [56].

of LDA powers greater than 170 W (and/or more spectrally-narrowed output) should lead to further increases in P_{max}, particularly at higher xenon loadings. The specification of the laser confined Dataset2 experiments to the 100 W to 170 W power range, but the simulations shown in Fig. 6 have no such limitation. Thus, extrapolated variants (laser powers of 25–1000 W) of displays Fig. 6 are presented in the ESI. If the increased heat load could be mitigated, greater LDA power would allow for operation in the regimes with higher [Rb], thereby increasing γ_{SEOP} and HP Xe production rates. A way to mitigate thermal issues that are exacerbated by high fluxes and high [Xe] may be the addition of more-thermally-conductive He to the SEOP mixture (this prospect is considered later with Sim2).

4.4. Optimal absorption trend

Upon examining the results of Sim2 it became clear that there was a distinct pattern in the amount of power absorption that occurred at P_{max} for a given gas mix at a given set of experimental conditions. For instance, at Dataset2 conditions – that is for a D = 2", L = 25 cm cell containing a binary gas mixture at a pressure of 2000 Torr irradiated with a 0.3 nm FWHM laser – optimal power absorption was constant at approximately ~63%; this is shown in Fig. 8. Here, $P_{Xe}, \langle P_{Rb} \rangle$, and % power absorbed are shown (blue, green, and red, respectively) for four selected Sim2 simulations of Dataset2 experimental conditions: 100 W of lasing power at 275 & 1000 Torr Xe ((a) & (c)); and 170 W of lasing power at 275 and 1000 Torr Xe ((b) & (d)). The blue vertical dashed lines indicate P_{max}, and the red horizontal dashed lines indicate the amount of laser absorption at P_{max}. Laser absorption in every case is ~63% regardless of power and [Xe] (62.88%, 63.34%, 62.41% and 62.88% for (a), (b), (c), and (d) respectively). Fig. 9 shows that this result holds for all of the gas mixes (275, 515, 1000, 1500, 2000 Torr Xe) and laser powers (100, 125, 142, 170 W) simulated under at Dataset2 (XeUS) conditions (solid lines with squares).

A similar pattern was observed when the simulation was taken beyond the ranges of conditions explored in Dataset2. For example, Fig. 9 shows % power absorbed as a function of [Xe] for the P_{max} values at various laser spectral widths (0.015, 0.15, 10 nm FWHM) and at various total gas pressures (0.25, 2 and 10 times the Dataset2 total gas pressure). Each group was simulated at four laser powers (100, 125, 142, 170 W) and 5 Xe fractions: 275, 515, 1000, 1500, and 2000 Torr (or equivalent fraction if the total gas pressure was modulated). In all cases but one, the plots indicate that the % absorption at P_{max} is independent of incident laser power, and virtually independent of [Xe] (only a very minor decrease with increasing [Xe] is evident). Indeed, simulating Dataset2 for a fixed Rb absorption linewidth, i.e. in the absence of pressure broadening (cf. Eq. (4)), largely eliminated this slight

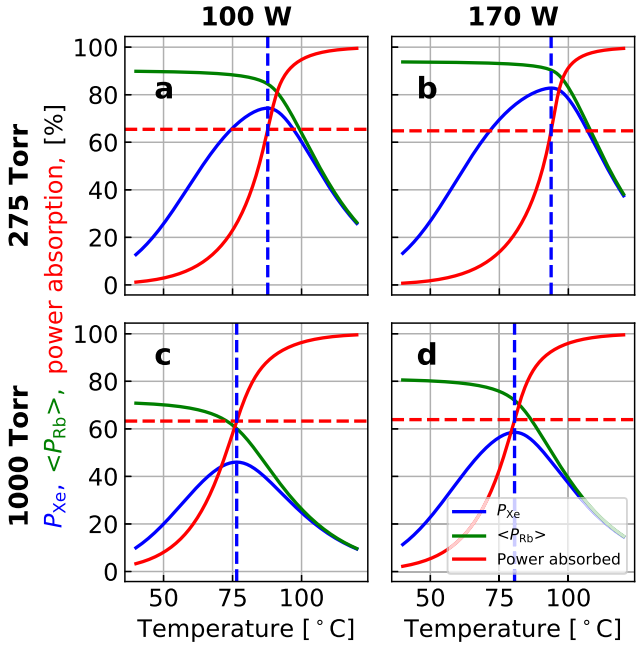

Fig. 8. Four selected Sim2 simulations of SF SEOP in a 2" cell with a total gas pressure of 2000 Torr and OP laser linewidth of 0.3 nm FWHM. Top and bottom rows are 275 and 1000 Torr of Xe respectively, backfilled with N_2. Left and right columns are 100 W and 170 W of incident OP laser power, respectively. Blue, green, and red, curves respectively show $\%P_{Xe}$, $\%P_{Rb}$, and % power absorbed, as functions of T. At P_{max} for each condition (vertical blue dashed lines), the % power absorbed is always ~63% (horizontal red dashed lines), i.e. virtually independent of [Xe] and laser power.

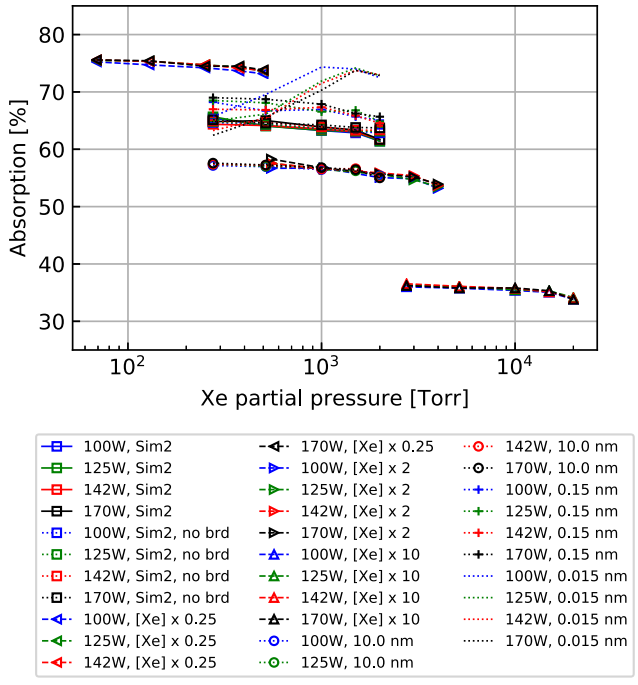

Fig. 9. Sim2 simulations of SF SEOP at 8 groups of conditions: 'Sim2' (Dataset2 conditions); 'Sim2, no brd' (explained below); Sim2 conditions but with 0.5, 2, and 10 times the Sim2 partial and total pressures; Sim2 conditions but with laser FWHM linewidths of 10, 0.15 and 0.015 nm. The plots show % laser power absorption at P_{max} (and thus T_{opt}) as a function of [Xe], here quantified using the partial pressure at loading at 25 °, for given variations of total pressure and laser spectral FWHM. 'Sim2, no brd' simulations are obtained using Sim2 but with an artificially fixed Rb D_1 linewidth such that no broadening is allowed to occur as a function of gas mix. Taken together, the plots indicate that % optimal power absorption is virtually independent of both incident laser power and [Xe] and for each group of conditions.

decrease with [Xe] (cf. Fig. 9 'Sim2, no brd')), supporting the conclusion that this slight dependence on [Xe] merely reflects a differential increase in pressure-broadening of the Rb line with increasing Xe. Only the 'ultra-narrow' 0.015 nm simulation at low [Xe] deviated from the absorption trend, exhibiting a lower absorption at P_{max}. This is likely because at low [Xe], we are closer to the limit of no Xe-induced Rb SD, so the effect of narrowing the laser linewidth (and coupling increasingly to the Rb D_1 and the temperature dependent Rb vapour density) dominates the behaviour of both P_{Rb} and P_{Xe} (in exactly the same way as for Sim2 simulations in Fig. 3). Further similar results – where cell geometry simulations are also plotted – are available in the ESI.

While the amount of laser absorption needed to achieve P_{max} is effectively constant for any given set of conditions examined (bar the ultra-narrow 0.015 nm case), the optimal absorption value changes as other experimental conditions are varied. For instance, considering first the total pressure modulation, there is a clear trend: As total pressure is increased from 0.25·[Xe] to 10·[Xe], the optimal absorption value decreases from ~75% to ~35%. For linewidth FWHM modulations (0.015, 0.15, 0.3, 10 nm) there is also a clear trend: 10 nm has the lowest optimal absorption value. This increases through ~63% for Dataset2 (XeUS) conditions (0.3 nm) to ~67% for 0.15 nm. This continues through to ~74% for 0.015 nm at higher [Xe], but at low [Xe] the optimal absorption at P_{max} is suppressed for reasons discussed above. Thus optimal absorption increases for decreasing linewidth. Again, further similar results for cell geometry simulations are available in the ESI.

4.5. Exploratory simulations: cell geometry, laser linewidth, total pressure, and addition of helium

Sim2 was used explore the parameter space surrounding Dataset2 and considered scenarios that could be readily implemented on, e.g., the XeUS line of SF SEOP polarisers [53–57,85]. In the results that follow, P_{Xe} is presented as a function of (1) buffer gas composition (Fig. 10); (2) cell geometry (Fig. 10); (3) laser linewidth (Figs. 10 and 11)); and (4) total gas pressure (Fig. 11). Dataset2 and the Sim2 simulations of Dataset2 are used as references in order to make comparisons. Table 3 summarises relevant parameters for each new simulation examined in this section.

For case (1), the simulations included a gas mixture wherein He comprised 90% of the buffer gas balance. As expected, replacing 90% of the N_2 buffer gas with He has ostensibly no impact on P_{Xe} when compared to the non-He simulations – in fact the curves in Fig. 10 overlap completely. Given this fact, He is likely a strong candidate to mitigate thermal issues that prevail during SEOP at high Xe density, high-photon-flux conditions because it is 28- and 6-fold more thermally conductive than Xe and N_2 respectively [86]. Indeed this outcome was observed in separate experiments that used *in situ* Raman spectroscopy to monitor in-cell SEOP temperatures [83]. Furthermore, the practice of using He as the dominant buffer gas could enable an increase in the operational duty cycle of SF polarisers via faster heating and cooling of the cells. Note however, that He cannot replace all of the N_2 within the cell

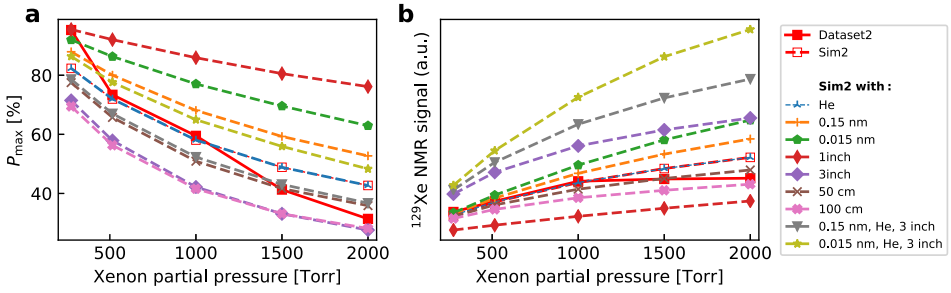

Fig. 10. Results of Sim2 simulations predicting (a) P_{max} (at T_{opt}) and (b) magnetisation (proportional to the NMR signal) as a function of modifications to Dataset2 conditions. Results include variations (and in some cases also combinations) of: (1) buffer gas (He comprising 90% of the buffer gas balance), (2) cell geometry (1, 2, and 3 inch cell diameters), and (3) OP laser spectral FWHM (0.015, 0.15, 0.3 nm FHWM). The solid red line with square markers is Dataset2. For each simulation, experimental parameters (e.g. cell length, area, T_1) were scaled appropriately and are summarised in Table 3.

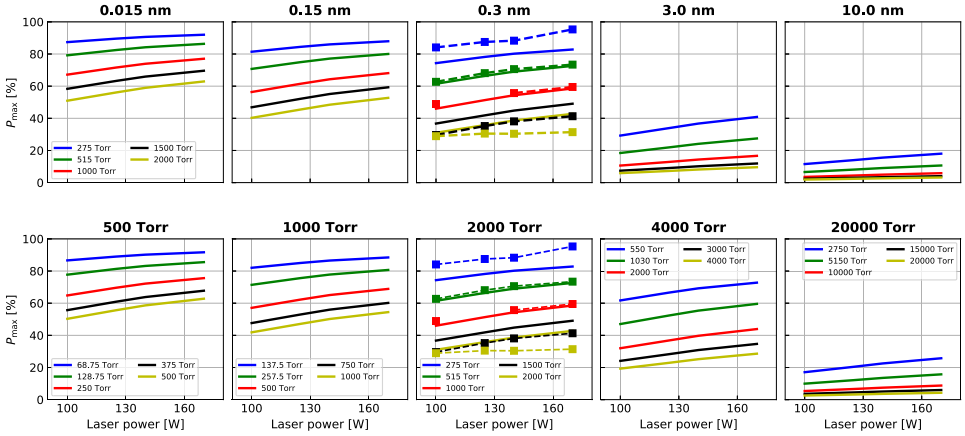

Fig. 11. Top row: P_{Xe} as a function of laser power and partial pressure for 5 different total pressures (corresponding to multiplying the Dataset2 total pressure by factors of 0.25, 0.5, 1.0, 2.0 and 10.0, respectively), as predicted by Sim2. Xe partial pressures correspond to 14, 26, 50, 75 and 90% of the total pressure indicated by the blue, green, red, black and gold lines respectively. Dashed lines with squares are experimental values (Dataset2). Bottom row: Optimal P_{Xe} as a function of laser power and Xe partial pressure at 5 laser FWHM linewidths: 0.015, 0.15, 0.3, 3, and 10 nm, as predicted by Sim2. [Xe] = 275, 515, 1000, 1500, and 2000 Torr are indicated by the blue, green, red, black, and yellow lines respectively. Dashed lines show corresponding values from Dataset2.

because N_2 provides a non-radiative pathway for the de-excitation of Rb atoms, ultimately preventing polarisation loss [87,43].

In case (2) 1" and 3" diameter OP cells were considered, along with 2" OP cells with increased L = 50 & 100 cm. Cell geometry determines i) how OP light is distributed throughout the cell, ii) the volume of gas to be polarised, and iii) the rate of wall induced relaxation (via the S/V ratio); a large S/V ratio will result in greater relaxation. Relative to the 2" cell, P_{Xe} in the 3" cell drops due to the dilution of incident flux, but magnetisation rises due to the larger cell volume. The 3" cell provides almost twice the signal of the 2" XeUS cell because increasing the diameter from 2" to 3" while keeping the length constant actually increases the cell volume by more than a factor of two. Using a 3" diameter cell will increase the net magnetisation generated, but unless cryo-collection or extraction methods other than positive pressure expansion (the current method) are employed (e.g. using large syringe pumps that can extract most of the contents of the cell after hyperpolarisation [60]), a significant fraction of HP gas will remain in the OP cell. The 3" cell may also run hotter than the 2" cell due to the reduced S/V ratio, increasing it's susceptibility to Rb runaway, though this effect could potentially be mitigated with the addition of He. A 1" cell enables high P_{Xe} values but the reduced volume results in low magnetisation. Both the 50 cm cell and the 100 cm cell fair worse than the Sim2 simulation of Dataset2 in terms of both P_{Xe} and magnetisation due to poorer light penetration. Correspondingly, T_{opt} becomes lower for these cells as the cell length increases in order to lower [Rb], and subsequently recover P_{Rb} at the back of the cell (that was low due to the poor light penetration).

For case (3) Dataset2 conditions were simulated for a range of incident pump laser spectral widths: 0.015, 0.15, 0.3, 3.0, and 10.0 nm FWHM. Reducing the laser linewidth from 0.3 nm to 0.15 and 0.015 nm (Fig. 10) increases both P_{Xe} and magnetisation, and disproportionally greater so for the higher [Xe] loadings, consistent with the Sim1 and Sim2 results shown previously in Fig. 3. Fig. 11 shows how P_{Xe} is expected to behave as a function of [Xe] and laser power for each of the laser FWHM listed. Again, as shown earlier in Fig. 3, greater P_{max} values can be expected at narrower linewidths.

Fig. 10 also shows the expected P_{Xe} and magnetisation trends with select cases of (1), (2), and (3) implemented simultaneously. The combination of a He-buffered, 3" OP cell, pumped with a 170 W, 0.015 nm FHWM laser gives the greatest magnetisation, thus investigations of this configuration are highly encouraged. While the thermal effects of He are not modelled here, its use is recommended on the grounds of its greater thermal conductivity that will likely be valuable in a 3 inch cell (with a lower S/V ratio) pumped with an ultra narrow 0.015 nm laser.

For case (4), Xe-rich SEOP is simulated as a function of the total pressure, with 5 total pressures considered – 500, 1000, 2000, 4000, and 20000 Torr – shown in Fig. 11. Xe partial pressures correspond to 14, 26, 50, 75 and 90% of the total pressure indicated by the blue, green, red, light blue and purple dashed lines respectively – the same proportions as Dataset2. Fig. 11 shows P_{max} decreases with pressure – a consequence of Γ_{SD}^{BC}.

5. Conclusions

High Xe density, high-photon-flux SF SEOP was simulated using two different simulation implementations, both of which draw on existing SEOP theory. Both validate well against Dataset1, reproducing the inverse relationship between T_{opt} and [Xe] with good quantitative agreement. Additionally, both implementations indicate that the possibility to polarise Xe to high levels at high [Xe] derives from the use of narrowed lasers and the exploitation of the T_{opt} relationship that maximises the photon-to-[Rb] ratio, and that the use of narrower linewidths should lead to further gains in HP Xe production. Sim2 was also compared to Dataset2 – a dataset that covered larger regions of parameter space at clinically-relevant production scales [56]. The simulation closely reproduces experimental P_{Xe}, γ_{SEOP}, and T_{opt} values over most of the parameter space and is thus considered to provide an excellent description of behaviour within the Xe-rich, high-photon-flux SF regime.

Exploratory simulations with Sim2 indicate a number of readily implementable options exist for increasing the magnetisation output – the product of the moles of Xe prepared and its polarisation– of clinical-scale SF (e.g. XeUS-type) polarisers. Of these, inclusion of He within the gas mixtures would likely be easiest to implement. Experimentally, this practice should increase thermal control – particularly at higher [Xe] where the greatest potential exists to increase magnetisation output if thermal issues can be addressed – and potentially increase the duty cycle of HP gas production due to the higher bulk thermal conductivity of the gas mixture. A 3" cell should double magnetisation output relative to the current 2" cell but require modification to parts of the polariser including: the optical train, the AR-coated windows, retro-reflector, and the 3D printed oven, all of which would be relatively easy to implement. However, for optimal results, a new gas extraction protocol may be required. Narrower laser linewidths will likely bring further gains in polariser output, particularly at Xe-rich mixtures with relatively low total pressures. Combining a He back-loaded, 3" cell (the largest considered here) with the narrowest possible laser should provide the best results.

Finally, scrutiny of the laser absorption revealed for the first time that in the SF configuration under the conditions examined, achieving the maximum P_{Xe} trends towards an optimal, fixed level of absorption that is effectively independent of laser power and [Xe] for a given laser linewidth, cell geometry, and total cell pressure, thereby providing a new method to rapidly optimise – and automate – SF Xe polarisers: For example, once P_{Xe} for one partial pressure has been maximised, all Xe partial pressures can be optimised by simply matching the integral of the laser power absorption spectrum to that obtained with the first optimisation. Implementation of the above improvements will be the subject of future efforts. Readers of this paper may also find of interest the results of a new simulation platform for CF SEOP created by Schrank (Ref. [88]).

Declaration of Competing Interest

The authors declare the following financial interests/personal relationships which may be considered as potential competing interests: Eduard Chekmenev, Boyd Goodson and Panayiotis Nikolaou each declare they have a stake in XeUS Technologies LTD. All other authors declare they have no conflict of interest.

Acknowledgements

We gratefully acknowledge the support of EPSRC, the School of Medicine, University of Nottingham, the NSF (CHE-1905341, CHE-1904780, CHE-1416432, CHE-1836308 and CHE-1416268), the NIH (1R21EB018014, 1F32EB021840, 1R21EB020323, 1R21CA220137), the NSF/DoD ASSURE Program (DMR-1757954), and the DOD (W81XWH-15–1-0271, W81XWH-15–1-0272, OISE-0966393, and W81XWH-12–1-0159/BC112431).

Appendix A. Supplementary material

Supplementary data associated with this article can be found, in the online version, at https://doi.org/10.1016/j.jmr.2020.106686.

References

[1] B.M. Goodson, N. Whiting, A.M. Coffey, P. Nikolaou, F. Shi, B.M. Gust, M.E. Gemeinhardt, R.V. Shchepin, J.G. Skinner, J.R. Birchall, et al., Hyperpolarization methods for MRS, eMagRes 4 (2015) 797–810.

[2] P. Nikolaou, B.M. Goodson, E.Y. Chekmenev, NMR hyperpolarization techniques for biomedicine, Chemistry–A, Eur. J. 21 (8) (2015) 3156–3166.

[3] T. Walker, W. Happer, Spin-exchange optical pumping of noble-gas nuclei, Rev. Mod. Phys. 69 (2) (1997) 629–642.

[4] T. Chupp, K. Coulter, Polarization of ^{21}Ne by spin exchange with optically pumped Rb vapor, Phys. Rev. Lett. 55 (10) (1985) 1074.

[5] G.E. Pavlovskaya, Z.I. Cleveland, K.F. Stupic, R.J. Basaraba, T. Meersmann, Hyperpolarized krypton-83 as a contrast agent for magnetic resonance imaging, Proc. Natl. Acad. Sci. USA 102 (51) (2005) 18275–18279.

[6] K.F. Stupic, Z.I. Cleveland, G.E. Pavlovskaya, T. Meersmann, Hyperpolarized ^{131}Xe NMR spectroscopy, J. Magn. Reson. 208 (1) (2011) 58–69.

[7] Y. Zheng, G.W. Miller, W.A. Tobias, G.D. Cates, A method for imaging and spectroscopy using γ-rays and magnetic resonance, Nature 537 (7622) (2016) 652.

[8] T. Chupp, M. Wagshul, K. Coulter, A. McDonald, W. Happer, Polarized, high-density, gaseous ^{3}He targets, Phys. Rev. C 36 (6) (1987) 2244.

[9] J.P. Mugler, B. Driehuys, J.R. Brookeman, G.D. Cates, S.S. Berr, R.G. Bryant, T.M. Daniel, E.E. De Lange, J.H. Downs, C.J. Erickson, W. Happer, D.P. Hinton, N.F. Kassel, T. Maier, C.D. Phillips, B.T. Saam, K.L. Sauer, M.E. Wagshul, MR imaging and spectroscopy using hyperpolarized ^{129}Xe gas: preliminary human results, Magn. Reson. Med. 37 (6) (1997) 809–815, https://doi.org/10.1002/mrm.1910370602.

[10] I. Dregely, J.P. Mugler, I.C. Ruset, T.A. Altes, J.F. Mata, G.W. Miller, J. Ketel, S. Ketel, J. Distelbrink, F. Hersman, et al., Hyperpolarized xenon-129 gas-exchange imaging of lung microstructure: first case studies in subjects with obstructive lung disease, J. Magn. Reson. Imaging 33 (5) (2011) 1052–1062.

[11] J.P. Mugler, T.A. Altes, Hyperpolarized ^{129}Xe MRI of the human lung, J. Magn. Reson. Imaging 37 (2) (2013) 313–331.

[12] K. Qing, K. Ruppert, Y. Jiang, J.F. Mata, G.W. Miller, Y.M. Shim, C. Wang, I.C. Ruset, F.W. Hersman, T.A. Altes, J.P. Mugler, Regional mapping of gas uptake by blood and tissue in the human lung using hyperpolarized xenon-129 MRI, J. Magn. Reson. Imaging 39 (2) (2014) 346–359, https://doi.org/10.1002/jmri.24181.

[13] L.L. Walkup, J.C. Woods, Translational applications of hyperpolarized ^{3}He and ^{129}Xe, NMR Biomed. 27 (12) (2014) 1429–1438.

[14] Z. Wang, S.H. Robertson, J. Wang, M. He, R.S. Virgincar, G.M. Schrank, E.A. Bier, S. Rajagopal, Y.C. Huang, T.G. O'Riordan, et al., Quantitative analysis of hyperpolarized ^{129}Xe gas transfer MRI, Med. Phys. 44 (6) (2017) 2415–2428.

[15] Y.V. Chang, MOXE: A model of gas exchange for hyperpolarized ^{129}Xe magnetic resonance of the lung, Magn. Reson. Med. 69 (3) (2013) 884–890, https://doi.org/10.1002/mrm.24304.

[16] I. Muradyan, J.P. Butler, M. Dabaghyan, M. Hrovat, I. Dregely, I. Ruset, G.P. Topulos, E. Frederick, H. Hatabu, W.F. Hersman, S. Patz, Single-breath xenon polarization transfer contrast (SB-XTC): implementation and initial results in healthy humans, J. Magn. Reson. Imaging 37 (2) (2013) 457–470, https://doi.org/10.1002/jmri.23823.

[17] S.D. Swanson, M.S. Rosen, B.W. Agranoff, K.P. Coulter, R.C. Welsh, T.E. Chupp, Brain MRI with laser-polarized ^{129}Xe, Magn. Reson. Med. 38 (5) (1997) 695–698.

[18] M. Rao, N.J. Stewart, G. Norquay, P.D. Griffiths, J.M. Wild, High resolution spectroscopy and chemical shift imaging of hyperpolarized ^{129}Xe dissolved in the human brain in vivo at 1.5 tesla, Magn. Reson. Med. 75 (6) (2016) 2227–2234.

[19] X. Zhou, Y. Sun, M. Mazzanti, N. Henninger, J. Mansour, M. Fisher, M. Albert, MRI of stroke using hyperpolarized ^{129}Xe, NMR Biomed. 24 (2) (2011) 170–175, https://doi.org/10.1002/nbm.1568.

[20] R.T. Branca, T. He, L. Zhang, C.S. Floyd, M. Freeman, C. White, A. Burant, Detection of brown adipose tissue and thermogenic activity in mice by hyperpolarized xenon MRI, Proc. Nat. Acad. Sci. 111 (50) (2014) 18001–18006.

[21] M.M. Spence, S.M. Rubin, I.E. Dimitrov, E.J. Ruiz, D.E. Wemmer, A. Pines, S.Q. Yao, F. Tian, P.G. Schultz, Functionalized xenon as a biosensor, Proc. Nat. Acad. Sci. 98 (19) (2001) 10654–10657.

[22] M.G. Shapiro, R.M. Ramirez, L.J. Sperling, G. Sun, J. Sun, A. Pines, D.V. Schaffer, V.S. Bajaj, Genetically encoded reporters for hyperpolarized xenon magnetic resonance imaging, Nat. Chem. 6 (7) (2014) 629–634.

[23] F.T. Hane, T. Li, P. Smylie, R.M. Pellizzari, J.A. Plata, B. DeBoef, M.S. Albert, In vivo detection of cucurbit [6] uril, a hyperpolarized xenon contrast agent for a xenon magnetic resonance imaging biosensor, Sci. Rep. 7 (2017) 41027.

[24] B.A. Riggle, Y. Wang, I.J. Dmochowski, A "smart" ^{129}Xe NMR biosensor for pH-dependent cell labeling, J. Am. Chem. Soc. 137 (16) (2015) 5542–5548.

[25] C. Boutin, E. Léonce, T. Brotin, A. Jerschow, P. Berthault, Ultrafast z-spectroscopy for ^{129}Xe NMR-based sensors, J. Phys. Chem. Lett. 4 (23) (2013) 4172–4176.

[26] R.M. Fairchild, A.I. Joseph, K.T. Holman, H.A. Fogarty, T. Brotin, J.-P. Dutasta, C. Boutin, G. Huber, P. Berthault, A water-soluble Xe@ cryptophane-111 complex exhibits very high thermodynamic stability and a peculiar ^{129}Xe NMR chemical shift, J. Am. Chem. Soc. 132 (44) (2010) 15505–15507.

[27] V. Roy, T. Brotin, J.-P. Dutasta, M.-H. Charles, T. Delair, F. Mallet, G. Huber, H. Desvaux, Y. Boulard, P. Berthault, A cryptophane biosensor for the detection of specific nucleotide targets through xenon NMR spectroscopy, ChemPhysChem 8 (14) (2007) 2082–2085.

[28] G. Huber, T. Brotin, L. Dubois, H. Desvaux, J.-P. Dutasta, P. Berthault, Water soluble cryptophanes showing unprecedented affinity for xenon: candidates as NMR-based biosensors, J. Am. Chem. Soc. 128 (18) (2006) 6239–6246.

[29] M. Kunth, C. Witte, A. Hennig, L. Schröder, Identification, classification, and signal amplification capabilities of high-turnover gas binding hosts in ultra-sensitive NMR, Chem. Sci. 6 (11) (2015) 6069–6075.

[30] S. Klippel, C. Freund, L. Schröder, Multichannel MRI labeling of mammalian cells by switchable nanocarriers for hyperpolarized xenon, Nano Lett. 14 (10) (2014) 5721–5726.

[31] Y. Wang, B.W. Roose, E.J. Palovcak, V. Carnevale, I.J. Dmochowski, A genetically encoded β-lactamase reporter for ultrasensitive ^{129}Xe NMR in mammalian cells, Angew. Chem. 128 (31) (2016) 9130–9133.

[32] E. Mari, P. Berthault, ^{129}Xe NMR-based sensors: biological applications and recent methods, Analyst 142 (18) (2017) 3298–3308.

[33] K. Jeong, C. Netirojjanakul, H.K. Munch, J. Sun, J.A. Finbloom, D.E. Wemmer, A. Pines, M.B. Francis, Targeted molecular imaging of cancer cells using MS2-based ^{129}Xe NMR, Bioconjug. Chem. 27 (8) (2016) 1796–1801.

[34] K.K. Palaniappan, R.M. Ramirez, V.S. Bajaj, D.E. Wemmer, A. Pines, M.B. Francis, Molecular imaging of cancer cells using a bacteriophage-based ^{129}Xe NMR biosensor, Angew. Chem. 125 (18) (2013) 4949–4953.

[35] B.M. Goodson, Nuclear magnetic resonance of laser-polarized noble gases in molecules, materials, and organisms, J. Magn. Reson. 155 (2002) 157.

[36] A. Oros, N. Shah, Hyperpolarized xenon in NMR and MRI, Phys. Med. Biol. 49 (20) (2004) R105–R153.

[37] A. Cherubini, A. Bifone, Hyperpolarised xenon in biology, Prog. Nucl. Magn. Reson. Spectrosc. 42 (1) (2003) 1–30.

[38] L. Schroeder, Xenon for NMR biosensing: Inert but alert, Physica Med. 29 (1) (2013) 3–16, https://doi.org/10.1016/j.ejmp.2011.11.001. http://www.sciencedirect.com/science/article/pii/S1120179711001384.

[39] B.M. Goodson, K. Ranta, J.G. Skinner, A.M. Coffey, P. Nikolaou, M. Gemeinhardt, D. Anthony, S. Stephenson, S. Hardy, J. Owers-Bradley, M.J. Barlow, E.Y. Chekmenev, The Physics of Hyperpolarized Gas MRI, Elsevier, 2017, pp. 23–46.

[40] D.A. Barskiy, A.M. Coffey, P. Nikolaou, D.M. Mikhaylov, B.M. Goodson, R.T. Branca, G.J. Lu, M.G. Shapiro, V.-V. Telkki, V.V. Zhivonitko, et al., NMR hyperpolarization techniques of gases, Chem.-A Eur. J. 23 (4) (2017) 725–751.

[41] M. Bouchiat, T. Carver, C. Varnum, Nuclear polarization in He-3 gas induced by optical pumping and dipolar exchange, Phys. Rev. Lett. 5 (8) (1960) 373–375, https://doi.org/10.1103/PhysRevLett. 5.373.

[42] S. Parnell, M. Deppe, J. Parra-Robles, J. Wild, Enhancement of ^{129}Xe polarization by off-resonant spin exchange optical pumping, J. Appl. Phys. 108 (6) (2010) 064908.

[43] B. Driehuys, G.D. Cates, E. Miron, K. Sauer, D.K. Walter, W. Happer, High-volume production of laser-polarized ^{129}Xe, Appl. Phys. Lett. 96 (12) (1996) 1668–1670.

[44] I.C. Ruset, S. Ketel, F. Hersman, Optical pumping system design for large production of hyperpolarized ^{129}Xe, Phys. Rev. Lett. 96 (2006) 053002.

[45] G. Norquay, S.R. Parnell, X. Xu, J. Parra-Robles, J.M. Wild, Optimized production of hyperpolarized ^{129}Xe at 2 bars for in vivo lung magnetic resonance imaging, J. Appl. Phys. 113 (4) (2013) 044908.

[46] M. Freeman, K. Emami, B. Driehuys, Characterizing and modeling the efficiency limits in large-scale production of hyperpolarized ^{129}Xe, Phys. Rev. A 90 (2) (2014) 023406.

[47] A.L. Zook, B.B. Adhyaru, C.R. Bowers, High capacity production of >65% spin polarized xenon-129 for NMR spectroscopy and imaging, J. Magn. Reson. 159 (2) (2002) 175–182.

[48] G. Schrank, Z. Ma, A. Schoeck, B. Saam, Characterization of a low-pressure high-capacity Xe-129 flow-through polarizer, Phys. Rev. A 80 (6) (2009) 063424, https://doi.org/10.1103/PhysRevA.80.063424.

[49] M.G. Mortuza, S. Anala, G.E. Pavlovskaya, T.J. Dieken, T. Meersmann, Spin-exchange optical pumping of high-density xenon-129, J. Chem. Phys. 118 (4) (2003) 1581–1584.

[50] M. Wagshul, T. Chupp, Optical pumping of high-density Rb with a broadband dye laser and GaAlAs diode laser arrays: application to ^{3}he polarization, Phys. Rev. A 40 (8) (1989) 4447.

[51] C. Flower, M. Freeman, M. Plue, B. Driehuys, Electron microscopic observations of Rb particles and pitting in ^{129}Xe spin-exchange optical pumping cells, J. Appl. Phys. 122 (2) (2017) 024902.

[52] N. Whiting, P. Nikolaou, N.A. Eschmann, B.M. Goodson, M.J. Barlow, Interdependence of in-cell xenon density and temperature during Rb/Xe-129 spin-exchange optical pumping using VHG-narrowed laser diode arrays, J. Magn. Reson. 208 (2) (2011) 298–304, https://doi.org/10.1016/j.jmr.2010.11.016.

[53] P. Nikolaou, A.M. Coffey, L.L. Walkup, B.M. Gust, N. Whiting, H. Newton, I. Muradyan, M. Dabaghyan, K. Ranta, G.D. Moroz, et al., Xena: An automated 'open-source' ^{129}Xe hyperpolarizer for clinical use, Magn. Reson. Imaging 32 (5) (2014) 541–550.

[54] P. Nikolaou, A.M. Coffey, L.L. Walkup, B.M. Gust, N. Whiting, H. Newton, S. Barcus, I. Muradyan, M. Dabaghyan, G.D. Moroz, M.S. Rosen, S. Patz, M.J. Barlow, E.Y. Chekmenev, B.M. Goodson, Near-unity nuclear polarization with an open-source ^{129}Xe hyperpolarizer for NMR and MRI, Proc. Natl. Acad. Sci. arXiv:http://www.pnas.org/content/early/2013/08/13/1306586110.full.pdf+html, doi:https://doi.org/10.1073/pnas.1306586110. http://www.pnas.org/content/early/2013/08/13/1306586110.abstract.

[55] P. Nikolaou, A.M. Coffey, L.L. Walkup, B.M. Gust, C.D. LaPierre, E. Koehnemann, M.J. Barlow, M.S. Rosen, B.M. Goodson, E.Y. Chekmenev, A 3D-printed high power nuclear spin polarizer, J. Am. Chem. Soc. 136 (4) (2014) 1636–1642.

[56] P. Nikolaou, A.M. Coffey, K. Ranta, L.L. Walkup, B.M. Gust, M.J. Barlow, M.S. Rosen, B.M. Goodson, E.Y. Chekmenev, Multidimensional mapping of spin-exchange optical pumping in clinical-scale batch-mode ^{129}Xe hyperpolarizers, J. Phys. Chem. B 118 (18) (2014) 4809–4816.

[57] P. Nikolaou, A.M. Coffey, M.J. Barlow, M.S. Rosen, B.M. Goodson, E.Y. Chekmenev, Temperature-ramped ^{129}Xe spin-exchange optical pumping, Anal. Chem. 86 (16) (2014) 8206–8212.

[58] B.M. Goodson, N. Whiting, H. Newton, J.G. Skinner, K. Ranta, P. Nikolaou, M.J. Barlow, E.Y. Chekmenev, Spin-exchange optical pumping at high xenon densities and laser fluxes: principles and practice, Royal Soc. Chem. (2015) 96–121.

[59] A. Fink, D. Baumer, E. Brunner, Production of hyperpolarized xenon in a static pump cell: numerical simulations and experiments, Phys. Rev. A 72 (5) (2005) 053411.

[60] M.S. Rosen, T.E. Chupp, K.P. Coulter, R.C. Welsh, S.D. Swanson, Polarized ^{129}Xe optical pumping/spin exchange and delivery system for magnetic resonance spectroscopy and imaging studies, Rev. Sci. Instrum. 70 (2) (1999) 1546–1552.

[61] K. Ranta, L. Walkup, N. Whiting, P. Nikolaou, M. Barlow, B. Goodson, Interplay of temperature, Xe density, and laser linewidth during Rb-Xe spin-exchange optical pumping: simulation vs. experiment, in: 52nd Experimental Nuclear Magnetic Resonance Conference 2011, Boston, USA, 2011.

[62] K. Ranta, Clinical-scale hyperpolarization of ^{129}Xe and ^{131}Xe via stopped-flow spin exchange optical pumping, Ph.D. thesis, Southern Illinois University Carbondale, 2016.

[63] M.V. Romalis, E. Miron, G.D. Cates, Pressure broadening of Rb D_1 and D_2 lines by ^{3}He, ^{4}He, N_2, and Xe. line cores and near wings, Phys. Rev. A 56 (1997) 4569–4578, https://doi.org/10.1103/PhysRevA.56.4569.

[64] D.A. Steck, Rubidium 85 D line data, 2008.

[65] B. Larson, O. Häusser, P. Delheij, D. Whittal, D. Thiessen, Optical pumping of Rb in the presence of high-pressure ^{3}He buffer gas, Phys. Rev. A 44 (5) (1991) 3108.

[66] C. Alcock, V. Itkin, M. Horrigan, Vapour pressure equations for the metallic elements: 298–2500 K, Can. Metall. Q. 23 (3) (1984) 309–313.

[67] A.B.-A. Baranga, S. Appelt, M. Romalis, C. Erickson, A. Young, G. Cates, W. Happer, Polarization of ^{3}He by spin exchange with optically pumped Rb and K vapors, Phys. Rev. Lett. 80 (13) (1998) 2801.

[68] M.E. Wagshul, T. Chupp, Laser optical pumping of high-density Rb in polarized ^{3}He targets, Phys. Rev. A 49 (5) (1994) 3854.

[69] W. Chen, T. Gentile, T. Walker, E. Babcock, Spin-exchange optical pumping of He-3 with Rb-K mixtures and pure K, Phys. Rev. A 75 (1) (2007) 013416.

[70] M. Bouchiat, J. Brossel, L. Pottier, Evidence for Rb-rare-gas molecules from the relaxation of polarized Rb atoms in a rare gas. experimental results, J. Chem. Phys. 56 (7) (1972) 3703–3714.

[71] I. Nelson, T. Walker, Rb-Xe spin relaxation in dilute Xe mixtures, Phys. Rev. A 65 (1) (2001) 012712.

[72] I.C. Ruset, Hyperpolarized ^{129}Xe production and applications, Ph.D. thesis, University of New Hampshire, 1999.

[73] G. Cates, R. Fitzgerald, A. Barton, P. Bogorad, M. Gatzke, N. Newbury, B. Saam, Rb-^{129}Xe spin-exchange rates due to binary and three-body collisions at high Xe pressures, Phys. Rev. A 45 (7) (1992) 4631.

[74] C.V. Rice, D. Raftery, Rubidium – xenon spin exchange and relaxation rates measured at high pressure and high magnetic field, J. Chem. Phys. 117 (12) (2002) 5632.

[75] Y.-Y. Jau, N.N. Kuzma, W. Happer, Magnetic decoupling of 129-Xe-Rb and 129-Xe-Cs binary spin exchange, Phys. Rev. A 67 (2) (2003) 022720.

[76] P. Nikolaou, N. Whiting, N.A. Eschmann, K.E. Chaffee, B.M. Goodson, M.J. Barlow, Generation of laser-polarized xenon using fiber-coupled laser-diode arrays narrowed with integrated volume holographic gratings, J. Magn. Reson. 197 (2) (2009) 249–254, https://doi.org/10.1016/j.jmr.2008.12.015.

[77] N. Whiting, P. Nikolaou, N. Eschmann, M. Barlow, B. Goodson, Effects of laser power, linewidth, and component gas densities on the polarization of xenon with fixed-frequency volume holographic grating (VHG)-narrowed laser diode arrays, in: 49th Exptl., Nucl. Magn. Reson. Conf., Asilomar, CA, 2008.

[78] N. Whiting, N.A. Eschmann, B.M. Goodson, M.J. Barlow, ^{129}Xe-Cs (D1, D2) versus ^{129}Xe-Rb (D_1) spin-exchange optical pumping at high xenon densities using high-power laser diode arrays, Phys. Rev. A 83 (2011) 053428.

[79] A. Couture, T. Clegg, B. Driehuys, Pressure shifts and broadening of the Cs D1 and D2 lines by He, N_2, and Xe at densities used for optical pumping and spin exchange polarization, J. Appl. Phys. 104 (9) (2008) 094912.

[80] N. Whiting, P. Nikolaou, N.A. Eschmann, M.J. Barlow, R. Lammert, J. Ungar, W. Hu, L. Vaissie, B.M. Goodson, Using frequency-narrowed, tunable laser diode arrays with integrated volume holographic gratings for spin-exchange optical pumping at high resonant fluxes and xenon densities, Appl. Phys. B: Lasers Opt. 106 (2012) 775–788, https://doi.org/10.1007/s00340-012-4924-x.

[81] D.K. Walter, W. Griffith, W. Happer, Energy transport in high-density spin-exchange optical pumping cells, Phys. Rev. Lett. 86 (15) (2001) 3264–3267.

[82] H. Newton, L.L. Walkup, N. Whiting, L. West, J. Carriere, F. Havermeyer, L. Ho, P. Morris, B.M. Goodson, M.J. Barlow, Comparative study of in situ N_2 rotational Raman spectroscopy methods for probing energy thermalisation processes during spin-exchange optical pumping, Appl. Phys. B: Lasers Opt. (2013), https://doi.org/10.1007/s00340-013-5588-x.

[83] J. Birchall, N. Whiting, J. Skinner, M.J. Barlow, B.M. Goodson, Using Raman Spectroscopy to Improve Hyperpolarized Noble Gas Production for Clinical Lung Imaging Techniques, InTech, 2017, pp. 247–268.

[84] C. Witte, M. Kunth, F. Rossella, L. Schröder, Observing and preventing rubidium runaway in a direct-infusion xenon-spin hyperpolarizer optimized for high-resolution hyper-CEST (chemical exchange saturation transfer using hyperpolarized nuclei) NMR, J. Chem. Phys. 140 (8) (2014) 084203.

[85] J.G. Skinner, Optimisation of xenon rich stopped flow spin-exchange optical pumping for functional lung imaging, Ph.D. thesis, University of Nottingham, 2017.

[86] G. Kaye, T. Laby, Tables of Physical and Chemical Constants, Longman Sc & Tech, 1995.

[87] I. Saha, P. Nikolaou, N. Whiting, B.M. Goodson, Characterization of violet emission from Rb optical pumping cells used in laser-polarized xenon NMR experiments, Chem. Phys. Lett. 428 (2006) 268–276.

[88] G.M. Schrank, A Novel, Finite-Element Model for Spin-Exchange Optical Pumping Using an Open-Source Code, arXiv:1911.01574 (2019).